



HAL
open science

Experimental evidence for wall-rock pulverization during dynamic rupture at ultra-high pressure conditions

Sarah Incel, Alexandre Schubnel, Jörg Renner, Timm John, Loïc Labrousse, Nadege Hilaiet, Helen Freeman, Yanbin Wang, François Renard, Bjørn Jamtveit

► To cite this version:

Sarah Incel, Alexandre Schubnel, Jörg Renner, Timm John, Loïc Labrousse, et al.. Experimental evidence for wall-rock pulverization during dynamic rupture at ultra-high pressure conditions. *Earth and Planetary Science Letters*, 2019, pp.115832. 10.1016/j.epsl.2019.115832 . hal-02319107

HAL Id: hal-02319107

<https://hal.univ-lille.fr/hal-02319107v1>

Submitted on 28 Sep 2020

HAL is a multi-disciplinary open access archive for the deposit and dissemination of scientific research documents, whether they are published or not. The documents may come from teaching and research institutions in France or abroad, or from public or private research centers.

L'archive ouverte pluridisciplinaire **HAL**, est destinée au dépôt et à la diffusion de documents scientifiques de niveau recherche, publiés ou non, émanant des établissements d'enseignement et de recherche français ou étrangers, des laboratoires publics ou privés.

1 **Experimental evidence for wall rock pulverization during dynamic rupture at ultra-high**
2 **pressure conditions**

3 Sarah Incel¹, Alexandre Schubnel², Jörg Renner³, Timm John⁴, Loïc Labrousse⁵, Nadège
4 Hilaiet⁶, Helen Freeman⁷, Yanbin Wang⁸, François Renard^{1,9}, and Bjørn Jamtveit¹

5
6 ¹Physics of Geological Processes, The Njord Centre, Department of Geosciences, University
7 of Oslo, Box 1048 Blindern, 0316 Oslo, Norway

8 ²Laboratoire de Géologie de l'ENS - PSL Research University - UMR8538 du CNRS, 24 Rue
9 Lhomond, 75005 Paris, France

10 ³Ruhr-Universität Bochum, Universitätsstraße 150, 44801 Bochum, Germany

11 ⁴Freie Universität Berlin, Institute of Geological Sciences, Malteserstr. 74-100, 12249 Berlin,
12 Germany

13 ⁵Sorbonne Université, CNRS-INSU, Institut des Sciences de la Terre Paris, IStEP, UMR
14 7193, 75005 Paris, France

15 ⁶Univ. Lille, CNRS, INRA, ENSCL, UMR 8207 - Unité Matériaux et Transformations,
16 59000 Lille, France

17 ⁷Helmholtz-Zentrum Potsdam, Deutsches GeoForschungsZentrum GFZ, Telegrafenberg,
18 14473 Potsdam, Germany

19 ⁸Center for Advanced Radiation Sources, the University of Chicago, Chicago, IL 60637, USA

20 ⁹Univ. Grenoble Alpes, Univ. Savoie Mont Blanc, CNRS, IRD, IFSTTAR,
21 ISTerre, 38000 Grenoble, France

22
23 *Correspondence to: sarah.incel@gmail.com

24 **Abstract**

25 The mechanisms triggering intermediate and deep earthquakes have puzzled geologists for
26 several decades. There is still no consensus concerning whether such earthquakes are
27 triggered by brittle or ductile mechanisms. We performed a deformation experiment on a
28 synthetic lawsonite-bearing blueschist at a confining pressure of 3 GPa and temperatures from
29 583 to 1,073 K. After deformation, the recovered sample reveals conjugated shear fractures.
30 Garnet crystals are dissected and displaced along these narrow faults and reveal micro- and
31 nanostructures that resemble natural pulverization structures as well as partial amorphization.
32 Formation of such structures is known to require strain rates exceeding 10^2 s^{-1} at low
33 confining pressures and is explained by the propagation of a dynamic shear rupture. The
34 absence of shearing in the pulverized wall rock is taken as evidence that these structures pre-
35 date the subsequent heat-producing frictional slip. In analogy to observations at low pressure
36 we infer that the garnet structures in our experiment result from rapid propagation of a shear
37 fracture even at the high pressure exerted on the sample and thus suggest that brittle
38 deformation is possible at lower crustal to upper mantle depths.

39

40 **Keywords:** pulverization, high-pressure deformation, dynamic rupture, lawsonite-blueschist,
41 DDIA apparatus, acoustic emissions

42 **1. Introduction**

43 During subduction at convergent plate margins, intermediate depth (70-300 km) and deep
44 (>300 km) earthquakes are common. Yet, the processes triggering earthquakes at the high
45 pressures (>1 GPa) prevailing at these depths are poorly understood. Both brittle (Raleigh and
46 Paterson, 1965; Kirby, 1987; Green II and Burnley, 1989; Dobson et al., 2002; Hacker et al.,

47 2003b; Schubnel et al., 2013; Okazaki and Hirth, 2016; Ferrand et al., 2017; Gasc et al., 2017;
48 Incel et al., 2017, 2019; and references therein) and ductile (Braeck and Podladchikov, 2007;
49 Kelemen and Hirth, 2007; John et al., 2009; Thielmann et al., 2015; Poli and Prieto, 2016;
50 Prieto et al., 2017; and references therein) mechanisms have been proposed.

51 While the suggested ductile mechanisms involve self-localizing failure by dissipative
52 heating and thermal runaway situations, the considered brittle mechanisms involve dynamic
53 rupture. In the former case, one expects significant shear deformation prior to seismic slip,
54 whereas in the latter case, wall rock damage may occur due to high strain rates and rapidly
55 changing stresses near a propagating rupture tip prior to frictional heating of the shear fracture
56 surfaces (Ben-Zion, 2003). Wall rock deformation associated with paleoearthquakes inferred
57 from the presence of pseudotachylytes, a rock type often assumed to be the result of frictional
58 melting and subsequent quenching (McKenzie and Brune, 1972; Sibson, 1975), was
59 interpreted as evidence for a thermal runaway mechanism (John et al., 2009; Deseta et al.,
60 2014). Studies of pseudotachylyte veins and their surrounding wall rocks in naturally
61 deformed rocks do, however, pose a number of challenges due to postseismic deformation and
62 recovery processes with respect to their formation (Guermani and Pennacchioni, 1998;
63 Mancktelow, 2006; Kirkpatrick and Rowe, 2013). Recent microstructural observations indicate
64 extremely high stresses in wall rocks around lower crustal earthquake zones, and abundant
65 fragmentation (Angiboust et al., 2012) without observable shear (Austrheim et al., 2017;
66 Petley-Ragan et al., 2018). Such fragmentation is often referred to as ‘pulverization’ when
67 occurring around faults in the shallow seismogenic regime and is assumed to result from
68 dynamic rupture processes (Dor et al., 2006; Mitchell and Faulkner, 2009; Rempe et al.,
69 2013).

70 In a previous experimental study, synthetic polycrystalline lawsonite-bearing blueschist
71 samples were deformed at confining pressures corresponding to lower crustal to upper mantle

72 depths (Incel et al. 2017). Faulting was accompanied by the record of acoustic emissions and
73 the growth of eclogite-facies minerals monitored using in-situ powder diffraction.
74 Examination of the recovered run products revealed several conjugated faults decorated with
75 nanocrystalline eclogite-facies transformation products in samples that entered the stability
76 field of eclogite. Therefore, Incel et al. (2017) suggested that failure occurred due to
77 transformation-induced instabilities, a mechanism titled transformational faulting (see also
78 Kirby, 1987; Green II and Burnley, 1989). In one of these samples (BS_3_1073 in Incel et al.
79 2017), garnet grains that are cut and displaced by the faults show microstructures similar to
80 what has been described from ‘pulverized’ garnets in natural fault rocks from lower crustal
81 lithologies (Austrheim et al., 2017; Petley-Ragan et al., 2018). Here, we further investigate the
82 micro- and nanostructure of different garnets found in this sample. In addition, we model the
83 spatial relation of the occurrence and absence of garnet fracturing relying on linear elastic
84 fracture mechanics with the aim to gain further insight into the nucleation and failure
85 mechanisms of intermediate-depth earthquakes.

86 **2. Experimental methods and analytical techniques**

87 2.1 Sample description and preparation of the starting material

88 A lawsonite-bearing blueschist from Alpine Corsica served as sample material. To avoid
89 any initial texture of the starting material a chemically homogeneous part of this blueschist
90 was crushed and sieved to a grain size $<38\ \mu\text{m}$. The major phases are glaucophane and
91 lawsonite in a ratio of $\sim 3:2$ making up $\sim 90\ \text{vol.}\%$ of the powder. Minor and accessory phases
92 are garnet, omphacite, actinolite, titanite, and phengite. The blueschist powder was hot-
93 pressed at 3 GPa and 923 K for 24 hours in a piston-cylinder and machined to approx. 2.1 mm
94 in diameter and 3 mm in height. After hot-pressing, the sample’s phases reveal a

95 homogeneous texture (Fig. 1a). In particular, the garnets are randomly distributed throughout
96 the sample as evidenced by the Mn-element distribution map (Fig. 1b).

97 2.2 D-DIA deformation experiment

98 A 9×9×8 mm sized amorphous Boron-epoxy cuboid was used as pressure medium for the
99 experiment performed using a D-DIA apparatus. The hot-pressed sample is located in the
100 middle of this cuboid, sandwiched between two gold foils and two alumina pistons, and
101 surrounded by a BN sleeve that is inserted into a graphite furnace.

102 The deformation apparatus is mounted on the GSECARS beamline at the Advanced
103 Photon Source, National Laboratory, Argonne, IL, USA. The use of synchrotron radiation
104 during deformation made it possible to calculate the differential stress as well as the strain and
105 the strain rate during deformation. Stress was calculated on lattice planes of glaucophane
106 using powder diffraction patterns that were taken every five minutes of the deforming sample
107 and the strain was measured by using radiographs of the sample that were also taken every
108 five minutes during deformation. Details of the stress and strain calculation are described by
109 Incel et al. (2017). Additionally, the D-DIA apparatus is equipped with an acoustic emission
110 (AE) system. Acoustic emissions were recorded using a sampling rate of 50 MHz and in
111 trigger mode with a trigger threshold of 250 mV on two channels. The duration of the largest
112 AEs recorded were in the range of a few hundred microseconds. Hence, the interval size over
113 which the stress measurements are made is around six magnitudes larger than the event
114 duration. Further details on the experimental and AE setup can be found in Wang et al.
115 (2003), Gasc et al. (2011), and Schubnel et al. (2013).

116 First, the sample assembly was loaded hydrostatically to a confining pressure (P_c) of 3 GPa
117 (here confining pressure P_c equals the least principal stress σ_3). Then, heating was initialized
118 by increasing the furnace power manually to reach a temperature of 583 K. The sample was
119 kept at these conditions for 30 min before deformation with a strain rate of approx. $5 \times 10^{-5} \text{ s}^{-1}$

120 commenced. While deformation of the sample proceeded, the power was increased in 10 W
121 steps to heat up the sample from initially 583 to 1073 K. Heating steps were initiated at 5, 12,
122 18, 20, 25, 30, and 35 % axial strain.

123 2.3 Analytical techniques

124 Microstructural analyses of the recovered sample were performed using a field-emission
125 scanning electron microscope (FE-SEM) with an acceleration voltage of 15 kV. To
126 investigate the nanostructure of this sample, three focused-ion beam (FIB) sections were cut
127 using a FEI-Helios G4 UC-Dual Beam system for imaging, analysis and transmission electron
128 microscopy (TEM). The nanostructural analyses were conducted using a FEI Tecnai TEM and
129 a Jeol JEM 2011 transmission electron microscope. For both machines, the acceleration
130 voltage was 200 keV.

131 **3. Results**

132 3.1 Mechanical data and acoustic emissions

133 During the first stage of deformation at a temperature of 583 K, the sample was strained by
134 5 % and the differential stress increased towards a peak stress of approx. 3 GPa, i.e. the level
135 of the confining pressure (Fig. 2). The differential stress decreased continuously during
136 syndeformational heating of the sample. A total axial strain of 40 % was accumulated by the
137 time the temperature reached 1073 K. In total 10 acoustic emissions were recorded between
138 10 to 19 % axial strain. Two events recorded at around 12 % and at approx. 19 % axial strain,
139 respectively, were large events almost reaching voltage saturation of the recording system (5
140 V).

141 3.2 Microstructural analyses

142 Microstructural investigations using the field-emission scanning electron microscope (FE-
143 SEM) revealed faults oriented at an angle of around 45° to the direction of the axial stress σ_1
144 crosscutting the entire sample (Fig. 3a). It is possible that either some of the fault-filling
145 material (gouge) of the major faults was lost during sample preparation or the fault surfaces
146 were separated during decompression. However, some relicts of gouge material are preserved
147 at the fault borders. These relicts show holes after interaction with the electron beam of the
148 SEM, implying that this material is poorly crystalline (Fig. 3c).

149 Two different types of garnets can be identified in the deformed sample, (i) garnet crystals
150 that are dissected and displaced along narrow faults ($<1 \mu\text{m}$ wide; Figs. 3c; 4a-c) and (ii)
151 unsheared garnet grains situated at some distance to the nearest fault (~ 0.5 to 1.5 mm ; Figs.
152 3b, 4d, e). Two example sets of displaced garnet parts show apparent shear displacements of
153 42 and $58 \mu\text{m}$, respectively (Figs. 3c; 4a). Back-scattered electron (BSE) imaging reveals that
154 the displaced garnet halves are fragmented into pieces with diameters $<1 \mu\text{m}$ (Figs. 3d; 4b)
155 and some of them were dragged along during slip (red arrow in Fig. 3d). Garnet grains located
156 further away from the fractures do not seem to be fragmented at this magnification in the
157 SEM (Figs. 3b; 4d, e).

158 3.3 Nanostructural analyses

159 Transmission electron microscope (TEM) analyses were performed at three different sites
160 (Fig. 3b, c) to investigate the nanometer-scale structures of: (i) the fault-gouge of the narrow
161 fault dissecting and displacing a garnet crystal, (ii) a garnet crystal that is cut by this narrow
162 fault, hereafter referred to as damage-zone garnet, and (iii) a garnet crystal located at a
163 minimum of $\sim 0.5 \text{ mm}$ from any fault, denoted as host-rock garnet. The fault-gouge contains
164 garnet crystals with sizes ranging from $<20 \text{ nm}$ to $\sim 100 \text{ nm}$. In bright field mode TEM

165 images, the material embedding the garnets appeared brighter than the garnet grains (Fig. 5a).
166 An electron diffraction pattern of this area showed a few diffraction spots but also a diffuse
167 halo (Fig. 5b) implying a combination of domains that have lost their long-range crystalline
168 order and crystals large enough to produce diffraction spots.

169 Scanning transmission electron microscopy (STEM) of the damage-zone garnet
170 demonstrates that this grain is completely shattered into small fragments (Figs. 5c, 6a)
171 surrounded by a fault-filling material exhibiting vesicles and idiomorphic crystals (Fig. 6a).
172 Using energy-dispersive spectroscopy (EDS) measurements these idiomorphic crystals were
173 identified as omphacite. The surrounding matrix mainly consists of Si, Al, Na, and Ca in
174 addition to O. The diffraction pattern obtained from a circular area with a diameter of ~ 500
175 nm in the shattered damage-zone garnet shows few large and several weak diffraction spots,
176 indicative of a polycrystalline material, together with a diffuse halo in its center (Fig. 5c, d).
177 This halo is less prominent than the one obtained from diffraction of the fault-gouge (Fig. 5b).
178 A bright field and a dark field mode image of the same area within the shattered damage-zone
179 garnet taken at high magnification document grain-size and crystal-orientation variation,
180 respectively (Fig. 6b, c). The bright field image shows several grains ranging in size from ~ 10
181 to ~ 50 nm in diameter (Fig. 6b). A quantitative determination of the grain-size distribution is
182 hampered by the abundant overlap of small grains. Lattice fringes are clearly visible locally
183 (Fig. 6c). However, the brightness variation in the corresponding dark-field mode image
184 suggests variable lattice orientation on the nanometer scale.

185 Nanostructural analysis of the host-rock garnet shows numerous fracture-like features and
186 possibly subgrains ranging in diameter from several hundred nanometers to $\sim 5 \mu\text{m}$ (Fig. 5e).
187 In contrast to the damage-zone garnet, though, very few grains have diameters < 100 nm (Fig.
188 5c, e). A diffraction pattern of an area with a diameter of ~ 500 nm (Fig. 5e) indicates a high
189 degree of crystallinity in this zone (Fig. 5f).

190 4. Discussion

191 4.1 Garnet pulverization due to dynamic rupture propagation

192 Our microscopic analyses revealed extensive fragmentation and grain-size reduction of the
193 damage-zone garnet. Its diffraction pattern shows numerous weak diffraction spots indicating
194 the presence of many small crystals. Additionally, a diffuse halo is observed implying that
195 some subdomains are either amorphous or too small (<10 nm) to produce well-defined
196 diffraction spots (Fig. 6c; Yund et al., 1990). On the contrary, the host-rock garnet is fully
197 crystalline and mainly reveals subgrain-formation (Fig. 5e, f). These experimental
198 microstructures are strikingly similar to what Austrheim et al. (2017) described as
199 “pulverization structures” in garnets found in close vicinity to a pseudotachylyte produced
200 during coseismic loading and faulting of granulites from the Bergen Arcs, Norway, and to
201 those found in garnets from mylonitic micaschists in the Sesia Zone, Swiss Alps (Trepmann
202 and Stöckhert, 2002).

203 Based on the record of acoustic emissions (Fig. 2), faulting and associated pulverization of
204 the wall rock occurred at a confining pressure of ~ 3 GPa, a differential stress of ~ 2.5 GPa, in
205 a temperature range from 640 to 720 K, at an experimentally imposed strain rate of $5 \times 10^{-5} \text{ s}^{-1}$
206 and at ~ 10 to 19 % axial strain. One characteristic feature of pulverized structures is the
207 absence or the low amount of shearing of the fragments (Trepmann and Stöckhert, 2002;
208 Austrheim et al., 2017). Due to the small fragment sizes of the damage-zone garnet it was not
209 possible to measure their orientation. It is likely that the fragments experienced some shearing
210 during further deformation as evidenced by the ‘tailing’ of the damage-zone garnet into the
211 fault (red arrow in Fig. 3d). However, because the fragments’ arrangement still mimics a
212 typical garnet crystal shape we can exclude significant shearing of the bulk crystals and their
213 environment (Figs. 3c, 4a, 5c). As evidenced by the microstructure of the recovered sample

214 showing lawsonite pseudomorphs as well as by in-situ monitoring of the mineral assemblage
215 during deformation, extensive reaction comprising the dehydration of lawsonite took place at
216 a later stage during deformation (Incel et al., 2017). Therefore, most of the remaining strain
217 was accommodated by lawsonite dehydration involving a solid volume change of around -
218 20 %.

219 When occurring at upper crustal depth (<15 km), wall-rock damage is explained by high
220 strain rates and stresses around a dynamically propagating rupture tip (Reches and Dewers,
221 2005; Dor et al., 2006; Doan and Gary, 2009; Mitchell et al., 2011; Bhat et al., 2012; Rempe
222 et al., 2013; Aben et al., 2017a, 2017b, 2016; Xu and Ben-Zion, 2017; Griffith et al., 2018).
223 Due to the much lower strength of rocks in tension than in compression, recently published
224 studies highlight the impact of isotropic or quasi-isotropic tension on the pulverization of
225 rocks (Xu and Ben-Zion, 2017; Griffith et al., 2018). In the model of Grady (1982) the author
226 quantifies the relation between the energy needed to create new fracture surfaces during
227 fragmentation and the inertial or kinetic energy available due to rapid loading. Later Glenn
228 and Chudnovsky (1986) added a strain energy term to this model that accounts for the energy
229 consumed by the solid until reaching its tensile strength. Based on this model, fragment size
230 will not vary over a wide range of strain rates (strain energy dominated regime). Once the
231 tensile strength of the material is exceeded, the fragment size exponentially decays with
232 increasing strain rate (kinetic energy dominated; Grady, 1982). Across natural faults, this
233 situation is realized in close distance (~5 cm) to the fault plane where strain rates are expected
234 to be high (Griffith et al. 2018). In the present study, we follow a similar approach as
235 presented in Griffith et al. (2018) in order to investigate, if the above model can explain the
236 observed difference in fragmentation intensity between the damage-zone and the host-rock
237 garnet. First, we check if the calculated fragment size matches our measured garnet fragments
238 using the Glenn and Chudnovsky (1986) model. Then, we test if the corresponding strain rates

239 fit the predicted strain rates around a dynamically propagating mode II crack tip at the
240 respective positions of the damage-zone and the host-rock garnet using linear elastic fracture
241 mechanics (see Freund, 1990). For these calculations, we used a density $\rho = 3,000 \text{ kg m}^{-3}$, a
242 garnet fracture toughness $K_{IC} = 1.5 \text{ MPa}$ (Mezeix and Green, 2006), and a range in garnet
243 tensile strength $\sigma^* = 433 \text{ MPa}$ to 4.3 GPa deduced using reported single crystal or aggregate
244 compressive strengths (Pardavi-Horváth, 1984; Kavner, 2007) assuming that the tensile
245 strength of a solid is around a third of its compressive strength. We used a shear modulus $\mu =$
246 64 GPa for glaucophane (Bezacier et al., 2010), a Poisson's ratio $\nu = 0.22$ (Cao et al., 2013),
247 and two different rupture velocities $v_r = 0.8c_s$ and $v_r = 0.9c_s$ with c_s being the shear wave
248 speed. The microstructural observations indicate a coseismic slip of a few tens of micrometer
249 (Figures 3c; 4a) corresponding to a range in fracture energy G_c of ~ 0.1 to 100 J m^{-2}
250 (Passelègue et al., 2016), deduced from experiments accounting for the uncertainty regarding
251 the critical slip distance (further explanations in Passelègue et al., 2016).

252 The calculated fragment size distribution matches quite well the measured garnet
253 fragments of the host-rock and the damage-zone garnet, respectively (Figures 5; 7a). Based on
254 linear elastic fracture mechanics, strain rates at the position of the host-rock garnet range from
255 $\sim 10^2$ to $\sim 10^4 \text{ s}^{-1}$ (Figure 7b). Combining the results of both calculations, the host-rock garnet
256 plots within the strain energy dominated regime (Figure 7). This fits well the nanostructural
257 analysis that reveals some fracture-like features, but mostly polygons that are homogeneously
258 sized resembling subgrains (Figures 5e; 8b). To explain the extensive fragmentation of the
259 damage-zone garnet, strain rates must have been high enough to exceed garnet's tensile
260 strength. Based on the measured fragment sizes of the damage-zone garnet, strain rates have
261 to be at least 10^8 s^{-1} (Figure 7a). Since the crack tip passed through this garnet crystal, such
262 high strain rates are realized within the damage-zone garnet volume in close vicinity to the
263 rupture tip (Figures 7b; 8a, b).

264 The theory of linear elastic fracture mechanics provides an asymptotic solution for a semi-
265 infinite crack that is only valid in the near-tip field (Freund, 1990). This requirement is
266 obviously difficult to satisfy regarding the length ratio of the shear fracture relative to the
267 respective garnet distances to the fault plane. A previous theoretical study on the relation
268 between wall-rock damage and depth reports an increase in the amount of fracture energy
269 dissipated in the off-fault medium with increasing depth (Okubo et al., 2019). The authors
270 also state that the width of the damage-zone decreases with depth. Consequently, this implies
271 that at deeper depth the off-fault damage will be confined to a narrow zone around the fault.
272 Showing extensively damaged garnets only in close vicinity to the fault, our experimental
273 study confirms these theoretical results.

274 4.2 Frictional melting of blueschist

275 Sliding of the fracture surfaces in mode II causes a temperature increase, which may
276 eventually lead to melting of the fracture surfaces. We deduce the presence of a solidified
277 melt from the amorphous material present in the fault-filling material (Fig. 5a,b) and in some
278 places intruded the shattered damage-zone garnet (Fig. 6a). In this “melting scenario”, the
279 vesicles in the amorphous material reflect fluid exsolution during decompression of the melt
280 and the observed idiomorphic omphacite crystals nucleate and grow during cooling of the
281 melt (Fig. 6a). Assuming a wet basalt solidus temperature T_s of $\sim 1,000$ K at ~ 3 GPa (Hacker
282 et al., 2003a), a sliding-related increase in temperature of 280-360 K over the temperatures
283 prevailing during the AE activity (640-720 K) would be sufficient to cause local melting.
284 After Cardwell et al. (1978), the temperature rise ΔT on a slipping fault can be expressed as

$$285 \quad \Delta T = \frac{\tau D}{\rho c_p \sqrt{\pi \kappa t_{\text{slip}}}} \quad (\text{eq. 1})$$

286 with shear stress τ , shear displacement D , density ρ , specific heat capacity c_p ($1,100 \text{ J kg}^{-1} \text{ K}^{-1}$
287 at $\sim 1,000$ K; Hartlieb et al., 2016), thermal diffusivity κ ($\sim 10^{-6} \text{ m}^2 \text{ s}^{-1}$), and slip duration t_{slip} .

288 The nominal shear stress τ and normal stress σ_n acting on the fault are ~ 1.25 GPa and 4.25
 289 GPa, respectively (with $\theta \approx 45^\circ$, $\sigma_1 = 5.5$ GPa, and $\sigma_3 = 3$ GPa). Assuming a minimum total
 290 displacement $D = 42 \mu\text{m}$ (Figs. 3c) and only 10 % of that slip to have happened coseismically
 291 and a sliding velocity of $\sim 1 \text{ m s}^{-1}$ (for a crack-like rupture; Schubnel et al., 2013) gives a slip
 292 duration t_{slip} of $\sim 4.2 \times 10^{-6}$ s. These estimates result in a ΔT of > 390 K indeed exceeding the
 293 difference between prevailing assembly temperature and the sample's solidus temperature.

294 The presence of a melt film on the fault surfaces can lead to fault lubrication (Di Toro et
 295 al., 2006). Dynamic shear strength τ_f of a fault with a continuous melt film strongly depends
 296 on the ratio between the width w of the molten zone that is filling the fault plane and the slip
 297 displacement (e.g., Ferrand et al., 2018)

$$298 \quad \tau_f = \frac{\rho[H + c_p \Delta T]w}{(1 - \eta)D} \quad (\text{eq. 2})$$

299 with the latent heat of fusion H ($\approx 3 \times 10^5 \text{ J K}^{-1}$) and the radiative efficiency η . In our sample,
 300 the narrow fault that contains molten material shows a width of $w \approx 100\text{-}500$ nm. Previous
 301 studies showed that the seismic efficiency, as function of the mechanical energy spent on slip
 302 during rupture, ranges between $0.1 < \eta < 0.5$ (Poli and Prieto, 2016). Within this span, equation
 303 (2) gives a dynamic shear strength of the fault as low as ~ 7 to 66 MPa (Fig. 9a) corresponding
 304 to friction coefficients of ~ 0.002 to 0.015 (Fig. 9b), i.e., significant lubrication (Figure 8c).

305 5. Conclusion and implications

306 The micro- and nanostructures observed in the damage-zone garnet, which resemble
 307 pulverization structures in natural rocks at upper as well as at lower crustal depths, can be
 308 explained by extensive fragmentation due to high strain rates associated with a dynamically
 309 propagating shear fracture. Such microstructures are not, however, compatible with fault
 310 models that involve failure by self-localizing thermal runaway mechanisms. In such a

311 situation, one would expect to see evidence of pre-failure shear strain in the wall rocks, and
312 the local differential stress levels should not rise above the initial externally imposed far-field
313 stress (John et al., 2009). However, it has been demonstrated that high local stresses, e.g., due
314 to coseismic loading, are required to fracture garnet (Trepmann and Stöckhert, 2002). After
315 the passage of the crack tip, frictional sliding of the fault surfaces causes melting and fault
316 lubrication. Our experimental study emphasizes the importance of dynamic rupture as a brittle
317 precursor to unstable frictional slip even at upper mantle depths.

318 **Acknowledgements**

319 The authors thank the two reviewers Greg Hirth and Ashley Griffith for their comments
320 and suggestions that helped improving the manuscript. The authors also thank Anja Schreiber
321 for the preparation of the FIB sections and Christian Chopin who provided the blueschist
322 sample. Special thanks to Frans Aben, François Passelègue, and Yehuda Ben-Zion for their
323 help and discussions and to Paul Meakin for a careful review of an early version of the
324 manuscript. The study received funding from the Alexander von Humboldt-foundation
325 (Feodor Lynen-fellowship to S.I.) and support from Geo.X in form of a travel Grant (to S.I.).
326 Further funding came from the People Program (Marie Curie Actions) of the European
327 Union's Seventh Framework Program FP7/2017-2013/ and Horizon 2020 under REA grant
328 agreements n° 604713 (to A.S.) and n° 669972 (to B.J.), EAR-1661489 for the development
329 of AE experiments (Y.W.). This research used resources of the Advanced Photon Source, a
330 U.S. Department of Energy Office of Science User Facility operated by Argonne National
331 Laboratory (contract n° DE-AC02-06CH11357). Financial support for H.M.F through
332 funding provided by the German Helmholtz Recruiting Initiative (award number I-044-16-01)
333 to Liane G. Benning from the GFZ is acknowledged.

334 **References**

- 335 Aben, F.M., Doan, M., Mitchell, T.M., Toussaint, R., Reuschlé, T., Fondriest, M., Gratier, J.,
336 Renard, F., 2016. Dynamic fracturing by successive coseismic loadings leads to
337 pulverization in active fault zones 121, 2338–2360. doi:10.1002/2015JB012542
- 338 Aben, F.M., Doan, M.L., Gratier, J.P., Renard, F., 2017a. AGU Monograph - Fault Zone
339 Dynamic Processes: Evolution of Fault Properties During Seismic Rupture, 1st ed,
340 Current. John Wiley & Sons, Inc.
- 341 Aben, F.M., Doan, M.L., Gratier, J.P., Renard, F., 2017b. High strain rate deformation of
342 porous sandstone and the asymmetry of earthquake damage in shallow fault zones. Earth
343 Planet. Sci. Lett. 463, 81–91. doi:10.1016/j.epsl.2017.01.016
- 344 Angiboust, S., Agard, P., Yamato, P., Raimbourg, H., 2012. Eclogite breccias in a subducted
345 ophiolite: A record of intermediatedepth earthquakes? *Geology* 40, 707–710.
346 doi:10.1130/G32925.1
- 347 Austrheim, H., Dunkel, K.G., Plümpner, O., Ildefonse, B., Liu, Y., Jamtveit, B., 2017.
348 Fragmentation of wall rock garnets during deep crustal earthquakes. *Sci. Adv.* 3, 1–7.
349 doi:10.1126/sciadv.1602067
- 350 Ben-Zion, Y., 2003. Appendix 2, Key Formulas in Earthquake Seismology. *Int. Handb.*
351 *Earthq. Eng. Seismol. Part B*, 1857–1875.
- 352 Bezacier, L., Reynard, B., Bass, J.D., Wang, J., Mainprice, D., 2010. Elasticity of
353 glaucophane, seismic velocities and anisotropy of the subducted oceanic crust.
354 *Tectonophysics* 494, 201–210. doi:10.1016/j.tecto.2010.09.011
- 355 Bhat, H.S., Rosakis, A.J., Sammis, C.G., 2012. A Micromechanics Based Constitutive Model
356 for Brittle Failure at High Strain Rates. *J. Appl. Mech.* 79, 31016.
357 doi:10.1115/1.4005897
- 358 Braeck, S., Podladchikov, Y.Y., 2007. Spontaneous thermal runaway as an ultimate failure

359 mechanism of materials. *Phys. Rev. Lett.* 98. doi:10.1103/PhysRevLett.98.095504

360 Cao, Y., Jung, H., Song, S., 2013. Petro-fabrics and seismic properties of blueschist and
361 eclogite in the North Qilian suture zone, NW China: Implications for the low-velocity
362 upper layer in subducting slab, trench-parallel seismic anisotropy, and eclogite
363 detectability in the subduction zone. *J. Geophys. Res. Solid Earth* 118, 3037–3058.
364 doi:10.1002/jgrb.50212

365 Cardwell, R.K., Chinn, D.S., Moore, G.F., Turcotte, D.L., 1978. Frictional Heating on a Fault
366 Zone With Finite Thickness. *Geophys. J. R. Astron. Soc.* 52, 525–530.
367 doi:10.1111/j.1365-246X.1978.tb04247.x

368 Deseta, N., Ashwal, L.D., Andersen, T.B., 2014. Initiating intermediate-depth earthquakes:
369 Insights from a HP-LT ophiolite from Corsica. *Lithos* 206–207, 127–146.
370 doi:10.1016/j.lithos.2014.07.022

371 Di Toro, G., Hirose, T., Nielsen, S., Pennacchioni, G., Shimamoto, T., 2006. Natural and
372 Experimental Evidence During Earthquakes. *Science* (80-.). 311, 647–649.
373 doi:10.1126/science.1121012

374 Doan, M.L., Gary, G., 2009. Rock pulverization at high strain rate near the San Andreas fault.
375 *Nat. Geosci.* 2, 709–712. doi:10.1038/ngeo640

376 Dobson, D.P., Meredith, P.G., Boon, S.A., 2002. Simulation of subduction zone seismicity by
377 dehydration of serpentine. *Science* (80-.). 298, 1407–1410.
378 doi:10.1126/science.1075390

379 Dor, O., Ben-Zion, Y., Rockwell, T.K., Brune, J., 2006. Pulverized rocks in the Mojave
380 section of the San Andreas Fault Zone. *Earth Planet. Sci. Lett.* 245, 642–654.
381 doi:10.1016/j.epsl.2006.03.034

382 Ferrand, T.P., Hilairet, N., Incel, S., Deldicque, D., Labrousse, L., Gasc, J., Renner, J., Wang,
383 Y., Green, H.W., Schubnel, A., 2017. Dehydration-driven stress transfer triggers

384 intermediate-depth earthquakes. *Nat. Commun.* 8, 1–11. doi:10.1038/ncomms15247

385 Ferrand, T.P., Labrousse, L., Eloy, G., Fabbri, O., Hilaiet, N., Schubnel, A., 2018. Energy
386 balance from a mantle pseudotachylyte, Balmuccia, Italy. *J. Geophys. Res. Solid Earth.*
387 doi:10.1002/2017JB014795

388 Freund, L.B., 1990. *Dynamic Fracture Mechanics*, Cambridge University Press.
389 doi:10.1017/CBO9780511546761

390 Gasc, J., Hilaiet, N., Yu, T., Ferrand, T., Schubnel, A., Wang, Y., 2017. Faulting of natural
391 serpentinite: Implications for intermediate-depth seismicity. *Earth Planet. Sci. Lett.* 474,
392 138–147. doi:10.1016/j.epsl.2017.06.016

393 Gasc, J., Schubnel, A., Brunet, F., Guillon, S., Mueller, H.J., Lathe, C., 2011. Simultaneous
394 acoustic emissions monitoring and synchrotron X-ray diffraction at high pressure and
395 temperature: Calibration and application to serpentinite dehydration. *Phys. Earth Planet.*
396 *Inter.* 189, 121–133. doi:10.1016/j.pepi.2011.08.003

397 Glenn, L.A., Chudnovsky, A., 1986. Strain-energy effects on dynamic fragmentation. *J. Appl.*
398 *Phys.* 59, 1379–1380.

399 Grady, D.E., 1982. Local inertial effects in dynamic fragmentation. *J. Appl. Phys.* 53, 322–
400 325. doi:10.1063/1.329934

401 Green II, H.W., Burnley, P.C., 1989. A new self-organizing mechanism for deep-focus
402 earthquakes. *Nature* 341, 733–737. doi:10.1038/341733a0

403 Griffith, W.A., St. Julien, R.C., Ghaffari, H.O., Barber, T.J., 2018. A Tensile Origin for Fault
404 Rock Pulverization. *J. Geophys. Res. Solid Earth* 123, 7055–7073.
405 doi:10.1029/2018JB015786

406 Guermani, A., Pennacchioni, G., 1998. Brittle precursors of plastic deformation in a granite:
407 an example from the Mont Blanc massif (Helvetic, western Alps). *J. Struct. Geol.* 20,
408 135–148. doi:10.1016/S0191-8141(97)00080-1

409 Hacker, B.R., Abers, G.A., Peacock, S.M., 2003a. Subduction factory 1. Theoretical
410 mineralogy, densities, seismic wave speeds, and H₂O contents. *J. Geophys. Res. Solid*
411 *Earth* 108, 1–26. doi:10.1029/2001JB001127

412 Hacker, B.R., Peacock, S.M., Abers, G.A., Holloway, S.D., 2003b. Subduction factory 2. Are
413 intermediate-depth earthquakes in subducting slabs linked to metamorphic dehydration
414 reactions? *J. Geophys. Res. Solid Earth* 108. doi:10.1029/2001JB001129

415 Hartlieb, P., Toifl, M., Kuchar, F., Meisels, R., Antretter, T., 2016. Thermo-physical
416 properties of selected hard rocks and their relation to microwave-assisted comminution.
417 *Miner. Eng.* 91, 34–41. doi:10.1016/j.mineng.2015.11.008

418 Incel, S., Hilairet, N., Labrousse, L., John, T., Deldicque, D., Ferrand, T.P., Wang, Y.,
419 Morales, L., Schubnel, A., 2017. Laboratory earthquakes triggered during eclogitization
420 of lawsonite-bearing blueschist. *Earth Planet. Sci. Lett.* 459, 320–331.
421 doi:10.1016/j.epsl.2016.11.047

422 Incel, S., Labrousse, L., Hilairet, N., John, T., Gasc, J., Shi, F., Wang, Y., Andersen, T.B.,
423 Renard, F., Jamtveit, B., Schubnel, A., 2019. Reaction-induced embrittlement of the
424 lower continental crust. *Geology* 47, 235–238. doi:https://doi.org/10.1130/G45527.1

425 John, T., Medvedev, S., Rüpke, L.H., Andersen, T.B., Podladchikov, Y.Y., Austrheim, H.,
426 2009. Generation of intermediate-depth earthquakes by self-localizing thermal runaway.
427 *Nat. Geosci.* 2, 137–140. doi:10.1038/ngeo419

428 Kavner, A., 2007. Garnet yield strength at high pressures and implications for upper mantle
429 and transition zone rheology. *J. Geophys. Res. Solid Earth* 112, 1–9.
430 doi:10.1029/2007JB004931

431 Kelemen, P.B., Hirth, G., 2007. A periodic shear-heating mechanism for intermediate-depth
432 earthquakes in the mantle. *Nature* 446, 787–790. doi:10.1038/nature05717

433 Kirby, S.H., 1987. Localized polymorphic phase transformations in high-pressure faults and

434 applications to the physical mechanism of deep earthquakes. *J. Geophys. Res. Solid*
435 *Earth* 92, 13789–13800. doi:10.1029/JB092iB13p13789

436 Kirkpatrick, J.D., Rowe, C.D., 2013. Disappearing ink: How pseudotachylytes are lost from
437 the rock record. *J. Struct. Geol.* 52, 183–198. doi:10.1016/j.jsg.2013.03.003

438 Mancktelow, N.S., 2006. How ductile are ductile shear zones? *Geology* 34, 345–348.
439 doi:10.1130/G22260.1

440 McKenzie, D., Brune, J.N., 1972. Melting on Fault Planes During Large Earthquakes.
441 *Geophys. J. R. Astron. Soc.* 29, 65–78. doi:10.1111/j.1365-246X.1972.tb06152.x

442 Mezeix, L., Green, D.J., 2006. Comparison of the mechanical properties of single crystal and
443 polycrystalline yttrium aluminum garnet. *Int. J. Appl. Ceram. Technol.* 3, 166–176.
444 doi:10.1111/j.1744-7402.2006.02068.x

445 Mitchell, T.M., Ben-Zion, Y., Shimamoto, T., 2011. Pulverized fault rocks and damage
446 asymmetry along the Arima-Takatsuki Tectonic Line, Japan. *Earth Planet. Sci. Lett.* 308,
447 284–297. doi:10.1016/j.epsl.2011.04.023

448 Mitchell, T.M., Faulkner, D.R., 2009. The nature and origin of off-fault damage surrounding
449 strike-slip fault zones with a wide range of displacements: A field study from the
450 Atacama fault system, northern Chile. *J. Struct. Geol.* 31, 802–816.
451 doi:10.1016/j.jsg.2009.05.002

452 Okazaki, K., Hirth, G., 2016. Dehydration of lawsonite could directly trigger earthquakes in
453 subducting oceanic crust. *Nature* 530, 81–84. doi:10.1038/nature16501

454 Okubo, K., Bhat, H.S., Rougier, E., Marty, S., Schubnel, A., Lei, Z., Knight, E.E., Klinger,
455 Y., 2019. Dynamics, radiation and overall energy budget of earthquake rupture with
456 coseismic off-fault damage. arXiv:1901.01771.

457 Pardavi-Horváth, M., 1984. Microhardness and brittle fracture of garnet single crystals. *J.*
458 *Mater. Sci.* 19, 1159–1170. doi:10.1007/BF01120025

459 Passelègue, F.X., Schubnel, A., Nielsen, S., Bhat, H.S., Deldicque, D., Madariaga, R., 2016.
460 Dynamic rupture processes inferred from laboratory microearthquakes. *J. Geophys. Res.*
461 *Solid Earth* 121, 4343–4365. doi:10.1002/2015JB012694

462 Petley-Ragan, A., Dunkel, K.G., Austrheim, H., Ildefonse, B., Jamtveit, B., 2018.
463 Microstructural Records of Earthquakes in the Lower Crust and Associated Fluid-Driven
464 Metamorphism in Plagioclase-Rich Granulites. *J. Geophys. Res. Solid Earth* 123, 3729–
465 3746. doi:10.1029/2017JB015348

466 Poli, P., Prieto, G.A., 2016. Global rupture parameters for deep and intermediate-depth
467 earthquakes. *J. Geophys. Res. Solid Earth* 121, 8871–8887. doi:10.1002/2016JB013521

468 Prieto, G.A., Froment, B., Yu, C., Poli, P., Abercrombie, R., 2017. Earthquake rupture below
469 the brittle-ductile transition in continental lithospheric mantle. *Sci. Adv.* 3, 1–6.
470 doi:10.1126/sciadv.1602642

471 Raleigh, C.B., Paterson, M.S., 1965. Experimental deformation of serpentinite and its tectonic
472 implications. *J. Geophys. Res.* 70, 3965–3985. doi:10.1029/JZ070i016p03965

473 Reches, Z., Dewers, T.A., 2005. Gouge formation by dynamic pulverization during
474 earthquake rupture. *Earth Planet. Sci. Lett.* 235, 361–374. doi:10.1016/j.epsl.2005.04.009

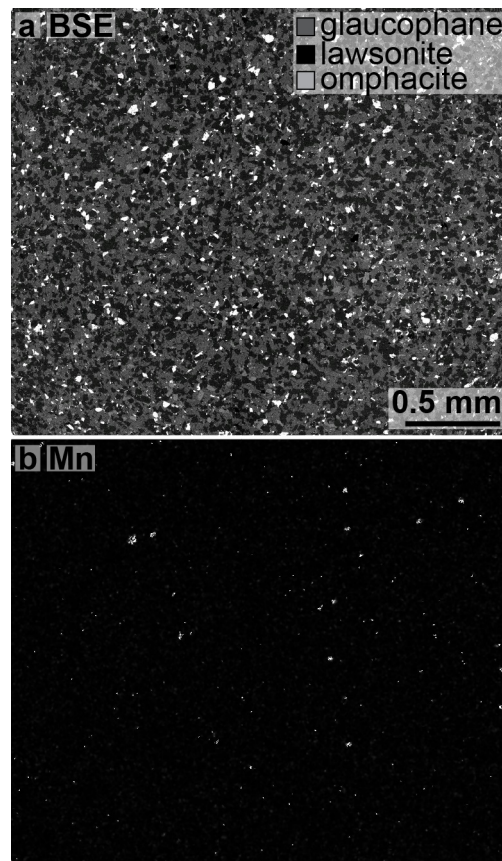
475 Rempe, M., Mitchell, T., Renner, J., Nippres, S., Ben-Zion, Y., Rockwell, T., 2013. Damage
476 and seismic velocity structure of pulverized rocks near the San Andreas Fault. *J.*
477 *Geophys. Res. Solid Earth* 118, 2813–2831. doi:10.1002/jgrb.50184

478 Schubnel, A., Brunet, F., Hilairet, N., Gasc, J., Wang, Y., Green, H.W., 2013. Deep-focus
479 earthquake analogs recorded at high pressure and temperature in the laboratory. *Science*
480 (80-.). 341, 1377–1380. doi:10.1126/science.1240206

481 Sibson, R.H., 1975. Generation of Pseudotachylyte by Ancient Seismic Faulting. *Geophys. J.*
482 *R. Astron. Soc.* 43, 775–794. doi:10.1111/j.1365-246X.1975.tb06195.x

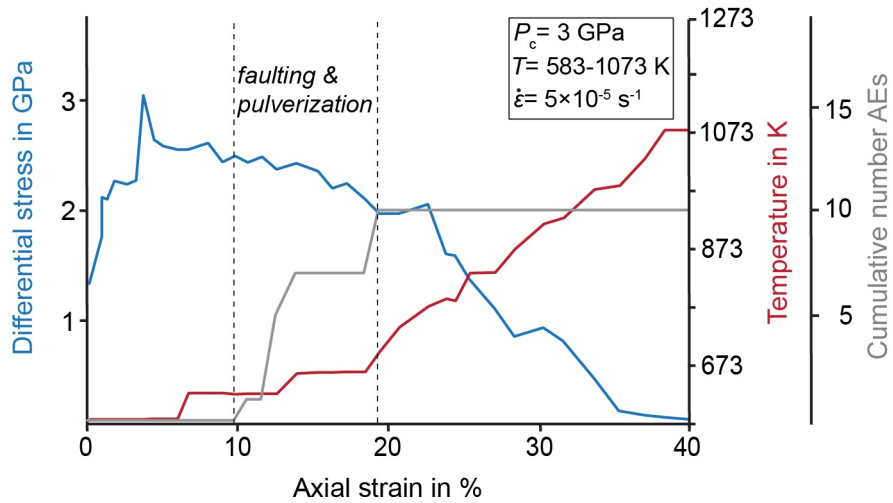
483 Thielmann, M., Rozel, A., Kaus, B.J.P., Ricard, Y., 2015. Intermediate-depth earthquake

484 generation and shear zone formation caused by grain size reduction and shear heating.
485 *Geology* 43, 791–794. doi:10.1130/G36864.1
486 Trepmann, C.A., Stöckhert, B., 2002. Cataclastic deformation of garnet: A record of
487 synseismic loading and postseismic creep. *J. Struct. Geol.* 24, 1845–1856.
488 doi:10.1016/S0191-8141(02)00004-4
489 Wang, Y., Durham, W.B., Getting, I.C., Weidner, D.J., 2003. The deformation-DIA: A new
490 apparatus for high temperature triaxial deformation to pressures up to 15 GPa. *Rev. Sci.*
491 *Instrum.* 74, 3002–3011. doi:10.1063/1.1570948
492 Xu, S., Ben-Zion, Y., 2017. Theoretical constraints on dynamic pulverization of fault zone
493 rocks. *Geophys. J. Int.* 209, 282–296. doi:10.1093/gji/ggx033
494 Yund, R.A., Blanpied, M.L., Tullis, T.E., Weeks, J.D., 1990. Amorphous Material in High
495 Strain Experimental Fault Gouges. *J. Geophys. Res.* 95, 15,589-15,602.
496



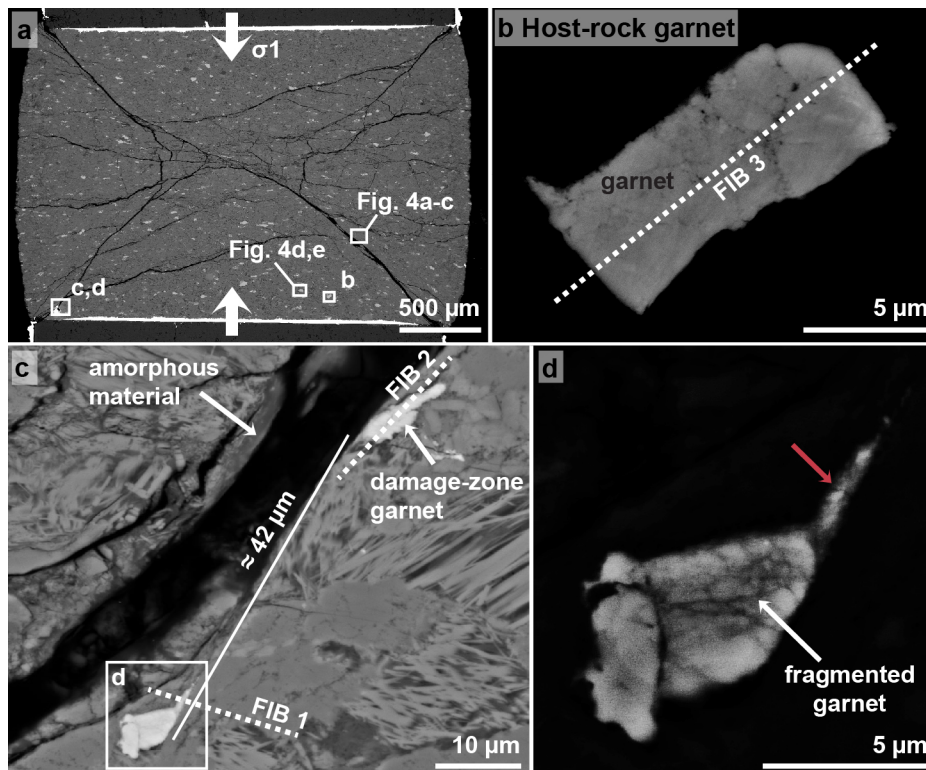
497

498 **Figure 1:** The starting material after hot-pressing. a) Backscattered electron (BSE) image
 499 showing that the phases are homogeneously distributed throughout the sample. b) A Mn-
 500 distribution map of the same region was used to highlight the location of garnet crystals.
 501



502

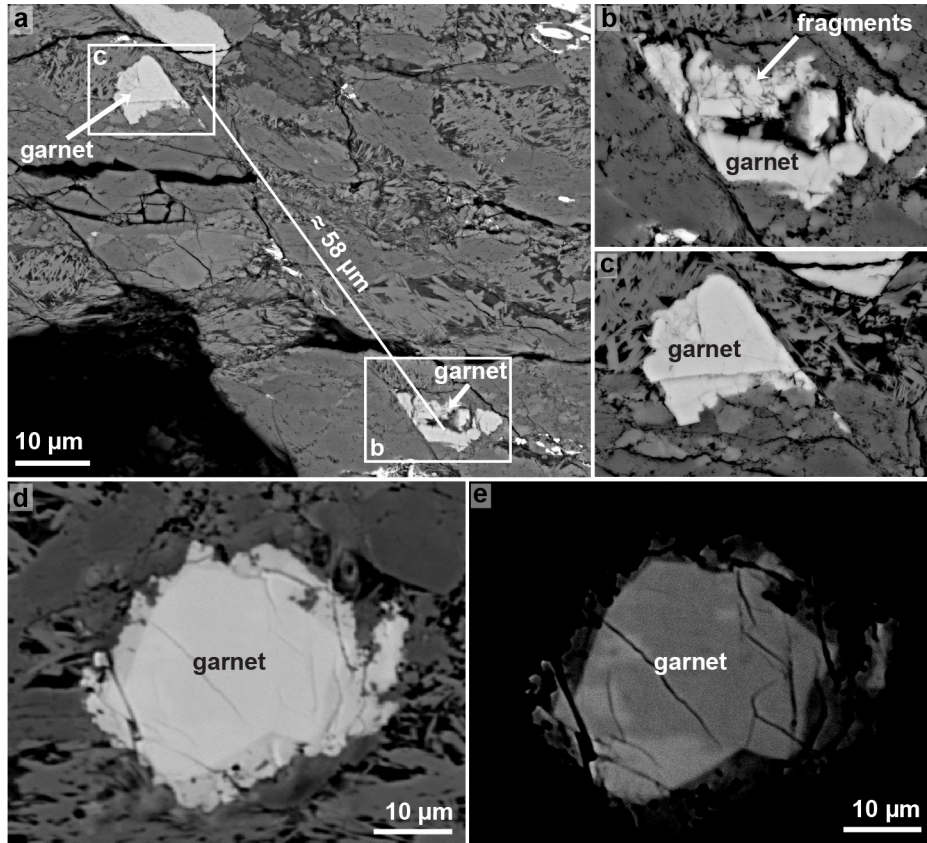
503 **Figure 2:** Differential stress, temperature, and cumulative number of acoustic emission (AE)
 504 events over axial strain. Based on the record of AEs (grey curve), faulting and pulverization
 505 occurs at a confining pressure (P_c)= 3 GPa, a differential stress of ~ 2.5 GPa (blue curve), in a
 506 temperature range of 640 to 720 K (red curve), at an imposed strain rate ($\dot{\epsilon}$) = $5 \times 10^{-5} \text{ s}^{-1}$, and
 507 an axial strain $\epsilon = \sim 10\text{-}19\%$.
 508



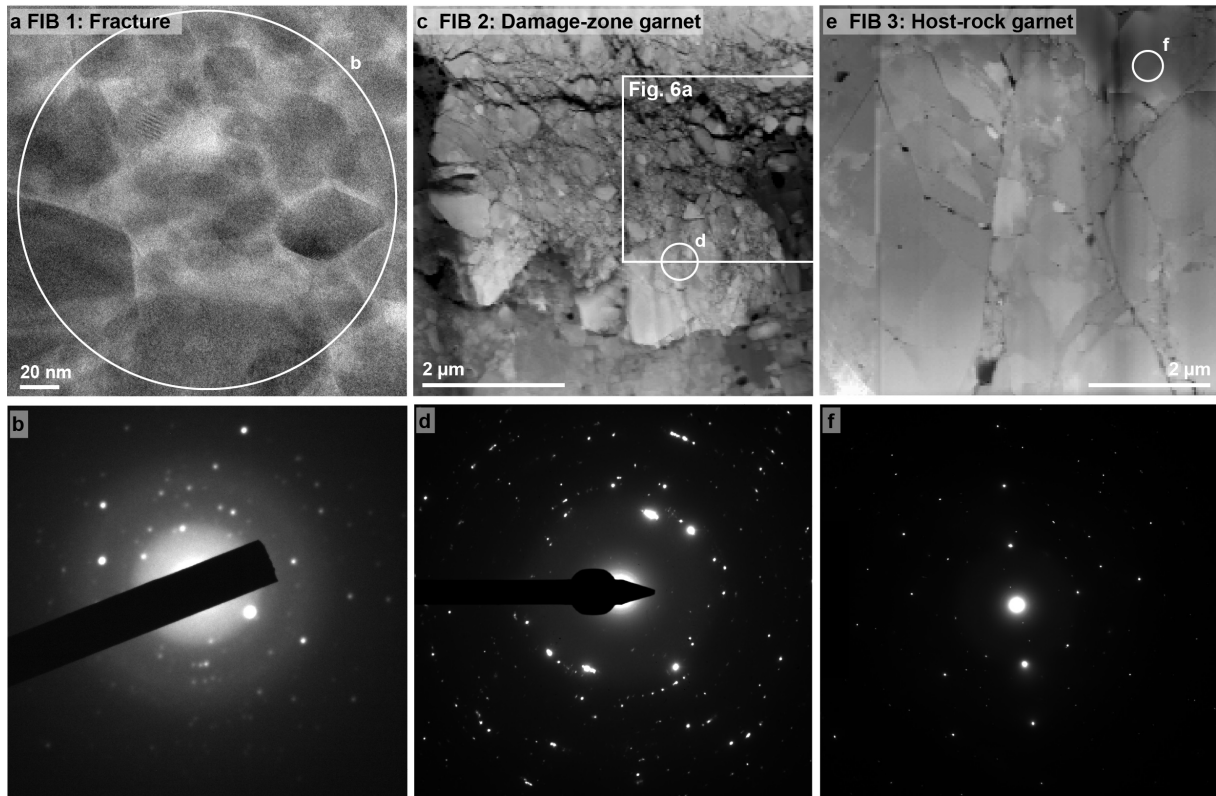
509

510 **Figure 3:** Backscattered electron images of the lawsonite-bearing blueschist sample after
 511 deformation. a) Overview image of the sample showing faults oriented at $\sim 45^\circ$ towards σ_1
 512 crosscutting the sample. The positions of the high-magnification images in b-d as well as the

513 position for Fig. 4 are highlighted with white rectangles, respectively. b) The host-rock garnet
 514 crystal that is located at $\sim 0.5 \mu\text{m}$ to the closest fault. The location of FIB section 3 is shown as
 515 white dashed line. c) A garnet pair that is dissected and displaced along a narrow fault. The
 516 apparent displacement is $\sim 42 \mu\text{m}$. The locations for FIB sections 1 and 2 are marked by white
 517 dashed lines. The white rectangle shows the location of a garnet half presented in d. d) At
 518 high magnification and high brightness contrast the garnet half appears fragmented into
 519 several pieces $< 1 \mu\text{m}$.
 520

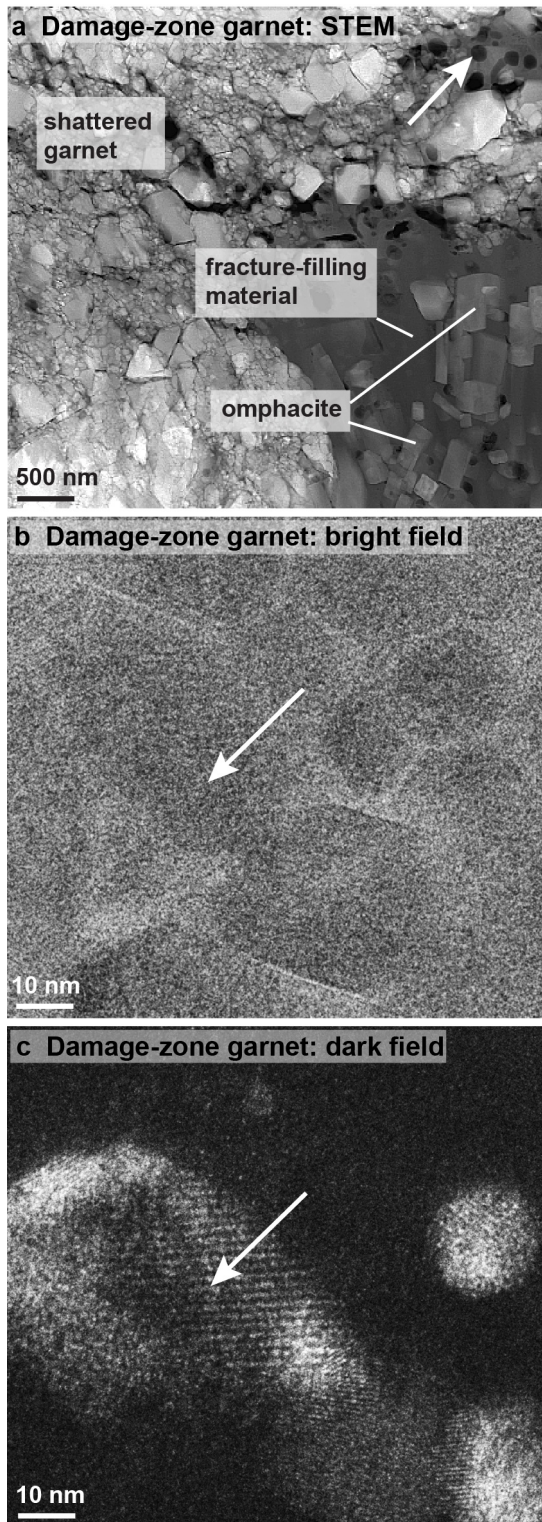


521
 522 **Figure 4:** a) Backscattered electron images of another pair of dissected and displaced crystals
 523 that are offset by a narrow fault. The offset along the narrow fault is $\sim 58 \mu\text{m}$. b and c) The
 524 two halves of the garnet pair showing extensive fragmentation in b). d and e) This garnet was
 525 found at $\sim 1 \text{ mm}$ from the nearest fault and seems relatively intact. e) Same crystal as in d)
 526 with the image taken at a higher brightness contrast at the SEM.
 527



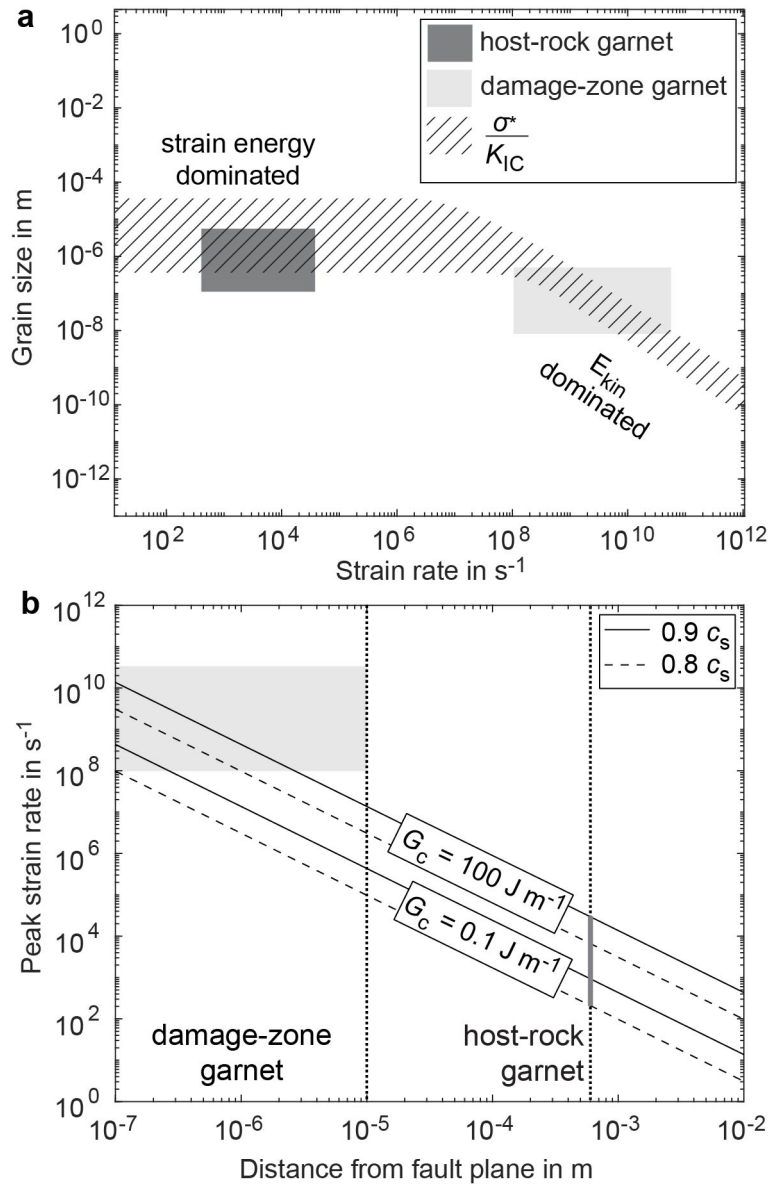
528

529 **Figure 5:** Transmission electron microscope images of the three FIB sections 1-3. a and b)
 530 FIB 1 revealing the fault-filling material. a) Bright field image showing dark (i.e. crystalline)
 531 garnet crystals floating in a bright (i.e. amorphous) material. The location chosen for a
 532 diffraction pattern is highlighted by a white circle. b) Diffraction pattern of the fault-filling
 533 material exhibiting few large and several weak diffraction spots and a diffuse halo. c and d)
 534 FIB section 2 cut across the damage-zone garnet next to the narrow fault. c) In STEM mode
 535 the damage-zone garnet appears to be completely shattered into pieces $<1 \mu\text{m}$. The white
 536 rectangle marks the position of Fig. 6a and the white circle shows the location of the
 537 diffraction pattern. d) Diffraction pattern of the shattered damage-zone garnet. Many weak
 538 diffraction spots indicate the presence of numerous small crystals. There is also a diffuse halo
 539 in the center of the diffraction pattern. e and f) FIB section 3 cut across the relatively intact
 540 host-rock garnet located at $\sim 0.5 \mu\text{m}$ from a fault. e) The fragments are much larger than those
 541 found in the damage-zone garnet. The white circle highlights the location chosen for a
 542 diffraction pattern. f) The diffraction pattern of the area shown in e) presents a crystalline
 543 structure.
 544



545

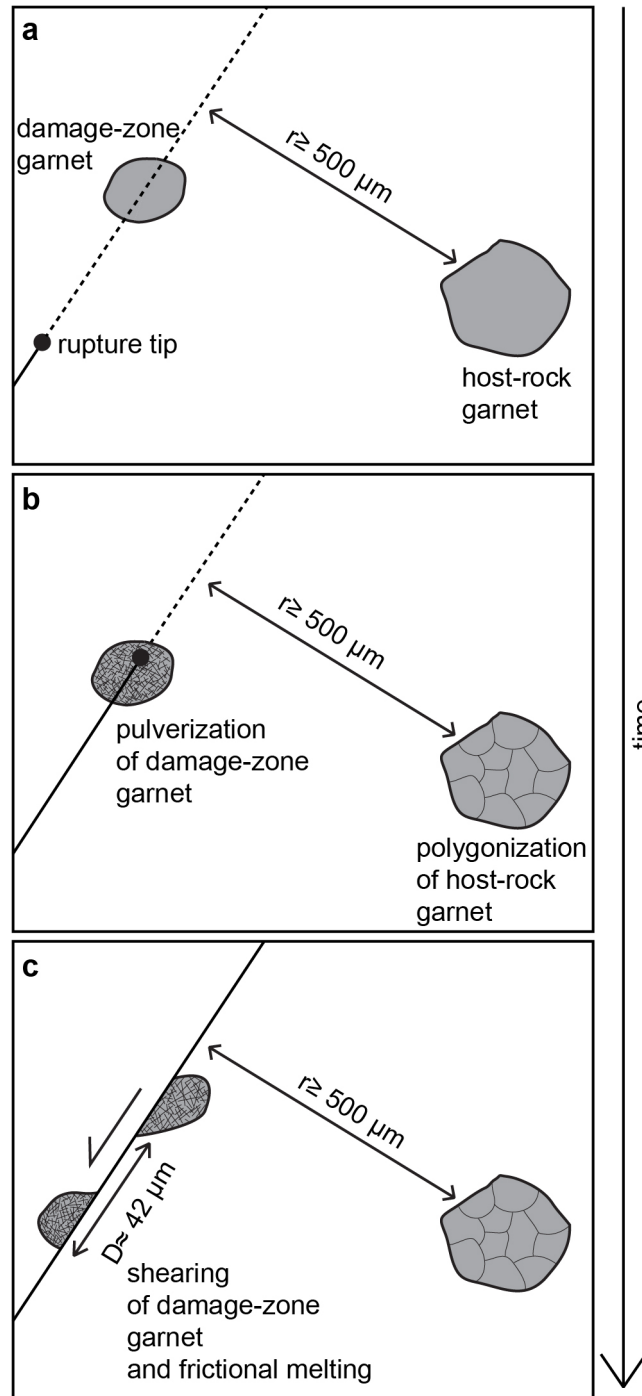
546 **Figure 6:** Transmission electron microscopy images of the shattered damage-zone garnet. a)
 547 STEM image revealing the fault-filling material surrounding the damage-zone garnet. Within
 548 this material vesicles (white arrow) and idiomorphic omphacite crystals can be found. b)
 549 Bright field image taken in the same zone as the diffraction pattern (Fig. 5c, d). c) The same
 550 area as shown in b) taken in dark field mode. The large grain marked by the white arrow
 551 shows subdomains (≤ 10 nm) that are slightly tilted.



552

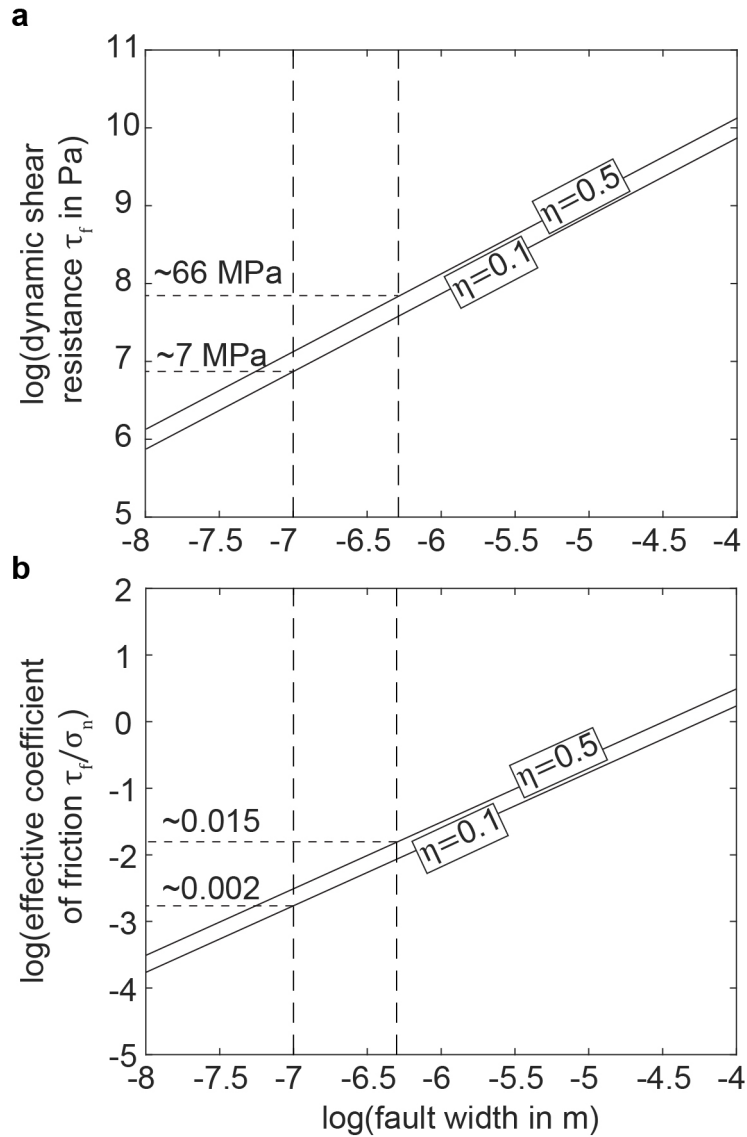
553 **Figure 7:** a) Grain size versus strain rate plot based on the models of Grady (1982) and Glenn
 554 and Chudnovsky (1986). The measured garnet fragments of the host-rock (dark grey
 555 rectangle) and the damage-zone garnet fragments (light grey rectangle) fit quite well the
 556 calculated fragment sizes (dashed area) over the investigated strain rate range. The minimum
 557 tensile strength for garnet aggregates is 433 MPa deduced from the compressive strength of
 558 garnet aggregates under confinement (Kavner, 2007). The maximum tensile strength was
 559 deduced from single crystal hardness measurements reported by Pardavi-Horváth (1984). For
 560 both we assumed that the tensile strength is around a third of the compressive strength. The
 561 fracture toughness of garnet is ~ 1.5 MPa (Mezeix and Green, 2006). b) Peak strain rates as a
 562 function of distance from the fault plane for two different rupture speeds v_r ($0.8c_s$ and $0.9c_s$)
 563 and two different fracture energies G_c (0.1 J m^{-1} and 100 J m^{-1} ; Passelègue et al., 2016).

564



565

566 **Figure 8:** a) Prior to rupture, both garnet crystals are intact. b) The rupture tip passes through
 567 the damage-zone garnet. Pulverization of the damage-zone garnet occurs due to the extreme
 568 strain rate around the crack tip (E_{kin} dominated Figure 7a). Because strain rate decays with
 569 distance, the host-rock garnet that is located at a minimum distance of $\sim 500 \mu\text{m}$ to the nearest
 570 fault only shows the formation of subgrains (strain energy dominated Figure 7a). c) Shearing
 571 behind the rupture tip causes the displacement of the garnet halves and eventually frictional
 572 melting of the fault surfaces.



573

574 **Figure 9:** a) Dynamic shear resistance and b) effective coefficient of friction versus width of
 575 the slip-associated melt layer. The vertical dashed lines mark the measured width of the
 576 molten zone filling out the fault along which a garnet pair is dissected and displaced (Fig. 3c).
 577 Recent studies show that the radiative efficiency increases with depth ranging between $\eta= 0.1$
 578 to 0.5 for intermediate depth earthquakes (50-300 km). The dashed horizontal lines indicate
 579 the intercept of this radiative efficiency range and the width range of the molten zone (~ 100 to
 580 500 nm) measured in the sample. The dynamic shear resistance would be ~ 7 to 66 MPa (a)
 581 resulting in an effective coefficient of friction of ~ 0.002 to 0.015 (b).